ARTICLES
https://doi.org/10.1038/s41561-020-0603-4
nature geoscience

Check for updates

Deep-sea eruptions boosted by induced fuel–coolant explosions

T. Dürig[1,2]✉, J. D. L. White[1], A. P. Murch[1,7], B. Zimanowski[3], R. Büttner[3], D. Mele[4], P. Dellino[4], R. J. Carey[5], L. S. Schmidt[6] and N. Spitznagel[3]

The majority of Earth's volcanic eruptions occur beneath the sea, but the limited number of direct observations and samples limits our understanding of these unseen events. Subaerial eruptions lend some insight, but direct extrapolation from the subaerial to the deep sea is precluded by the great differences in pressure, thermal conditions, density and rheology, and the interplay among them. Here we present laboratory fragmentation experiments that mimic deep-sea explosive eruptions and compare our laboratory observations with those from the kilometre-deep submarine eruption of Havre Volcano, Kermadec Arc, New Zealand, in 2012. We find that the Havre eruption involved explosive fragmentation of magma by a pressure-insensitive interaction between cool water and hot magma, termed an induced fuel–coolant interaction. The laboratory experiments show that this water–magma interaction is initiated by the formation of cracks in cooling magma into which the water coolant can infiltrate, driving explosive fragmentation. Explosive submarine eruptions have previously been considered unlikely because stabilization of a vapour film at the magma–water contact was thought to be a key requirement but is suppressed at depths exceeding 100 m. However, here we demonstrate that these induced fuel–coolant interactions between magma and water can occur in a range of wet environments regardless of pressure, from the subaerial to the deep sea, and may operate on different planets, as well as apply to materials other than magma and water.

The 2012 eruption of Havre Volcano, Kermadec Arc, New Zealand, produced in a day an ~400 km² pumice raft[1–3], and on the seafloor an abundance of fine ash[4]. Over 35 km² on the volcano, the ash, most widely distributed from the main eruptive phase, shows no thinning trend, so the total volume of erupted ash must substantially exceed the 100 million m³ in the mapped area[4]. We focus on ash (S1, S2) from this main phase[4]; it signals expenditure of a large amount of energy to fragment magma[5], which is surprising at this depth[6–8]. The ash, erupted from 900–1,100 m below sea level (b.s.l.), has abundant blocky or curviplanar-shaped particles <125 µm with low vesicularity and stepped fracture surfaces. Abundant fine to very fine ash suggests explosive fragmentation[9], but particle shapes are not those of pumiceous ash produced by the expansion of magmatic gases. Instead, we find fingerprints like those from fuel–coolant (thermohydraulic) ash-forming explosions. Havre is too deep, and rhyolite too viscous, for 'normal' fuel–coolant interactions[6,7,10–18], and we infer fragmentation by induced fuel–coolant interaction (IFCI). Experimental evidence is presented for its role at Havre. We suggest that IFCI aids ash production and increases explosivity during most submarine eruptions, and for deep-water volcanic eruptions it is probably the dominant ash-forming process.

MFCI and IFCI as kindred explosive processes

In volcanology, highly explosive energy release from the interaction of magma with water (molten fuel–coolant interaction (MFCI)) is known as the driving mechanism for subaerial, mostly basaltic, phreatomagmatic eruptions[10,11,19–22]. The key MFCI process is a non-equilibrium thermohydraulic feedback cycle (Fig. 1). Heat transferred from hot fuel into entrapped, expandable coolant induces strong hydraulic pressure on the fuel–coolant interface, creating brittle fractures that penetrate the fuel. Expanding liquid coolant pushes into these cracks, driving within fractions of milliseconds their further propagation, which increases the interface area, accelerates heat transfer and releases strong shock waves. The feedback persists until the system is opened and the superheated entrapped coolant is released as expanding vapour, carrying away with high kinetic energy the crack-bounded fragments.

In a study on Tepexitl[23], a desert volcano, it was experimentally verified that explosive fuel–coolant interaction processes are possible even for a highly viscous magma, and without water entrapment. Here we distinguish two conceptual models (Fig. 1) for fuel–coolant interaction and introduce the term IFCI as distinct from the well-explored 'regular' MFCI mechanism. The differences between these two are particularly relevant for submarine eruptive settings below the depth of stable film boiling (>1 MPa, deeper than 100 m b.s.l.[8,16]), and we show that IFCI produced most Havre 2012 ash using experiments, particle morphology, and thermodynamic analysis. This changes our view of deep-submarine eruptions, for which it is a deeply embedded concept that magma–water explosivity is unimportant.

IFCIs function by 'shortcutting' initiation of the thermohydraulic feedback loop, which is the underappreciated core of MFCI explosions. IFCI occurs when coolant enters cracks that open in a fuel being fragmented by other processes. While resembling the MFCI process in how heat is thermohydraulically converted in a feedback loop (Fig. 1) to release fragmentation energy, IFCI does not require vapour films and occurs under less restrictive initial and boundary conditions. On the basis of our analysis of initial threshold conditions, experiments and heat transfer simulations, we show that IFCI,

[1]Geology Department, University of Otago, North Dunedin, New Zealand. [2]Institute of Earth Sciences, University of Iceland, Reykjavík, Iceland. [3]Physikalisch Vulkanologisches Labor, Universität Würzburg, Würzburg, Germany. [4]Dipartimento di Scienze della Terra e Geoambientali, University of Bari, Bari, Italy. [5]School of Natural Sciences, University of Tasmania, Hobart, Tasmania, Australia. [6]Department of Geosciences, University of Oslo, Oslo, Norway. [7]Present address: National Museum of Nature and Science, Tokyo, Japan. ✉e-mail: tobi@hi.is

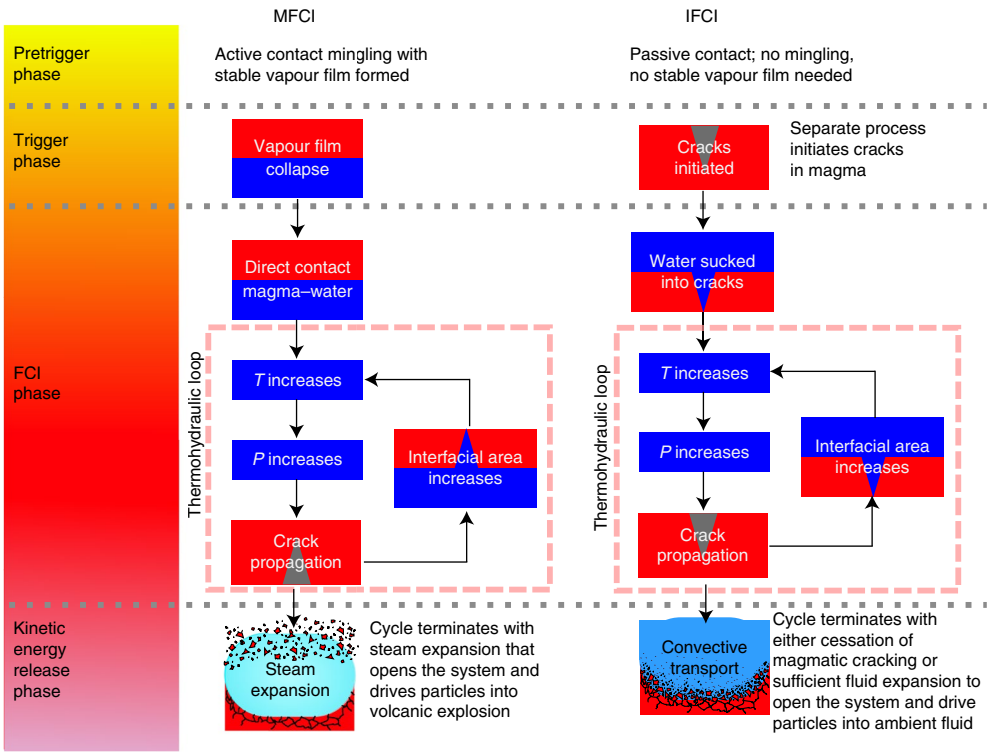

Fig. 1 | Comparison of MFCI with IFCI. Magma (red) is volcanic fuel, and water (blue) is the coolant. MFCI needs a pretrigger vapour film, limiting it to shallow water depths. IFCI initiation requires a sudden increase of the fuel's surface via cracking, for example, by brittle failure of magma highly strained during eruption.

here first diagrammed and established as a separate fuel–coolant process, can convert heat to produce ash in submarine eruptions at any depth.

We investigated IFCI characteristics and explored its role in the 2012 Havre eruption by conducting two series of fragmentation experiments with crushed and remelted Havre rock together with statistical ash sampling strategies (Methods). In 'dry' runs, melt was deformed and fragmented by injecting pressurized gas, whereas in IFCI runs, a layer of water was added before gas injection (Fig. 2). In IFCI runs, fragments were produced by (1) dry gas-driven cracking and (2) thermohydraulic processes during IFCI ('IFCI particles'). Thermohydraulic IFCI processes advanced downward in our setup, tracing the opening tensional cracks from the top of the melt (Methods). IFCI particles were thus much more abundant in the leading part of the ejected cloud of fragments than in the following ejecta. In both dry and IFCI runs, ejecta was collected from the ground ('DG' and 'IG' for dry and IFCI runs, respectively). IFCI products were also captured in a water bowl positioned alongside the open conduit, and as deposits inside water droplets ('IW') adhering to the walls and ceiling around the experimental area (Extended Data Fig. 1). Furthermore, in a novel subseries of IFCI experiments, one end of a U-shaped tube was mounted above the crucible with its other end leading to a water bowl. In these 'U-tube' runs, the tube detached ~30 ms after particle ejection began (Methods), dynamically separating the leading front of fine particles ('IU', Fig. 2).

We compared the shape of the ash-sized experimental products with natural ash retrieved at six locations close to Havre volcano, labelled 'Nat1' to 'Nat6' (Extended Data Fig. 1).

IFCI versus dry fragmentation experiments

The effect of IFCI on fragmentation is evident if the maximum recoil force F_{max} (that is, the repulsion force exerted on the crucible) is normalized relative to the maximum pressure P_{max} and plotted over itself (Fig. 3). Dry runs plot below the dashed line, while most IFCI runs plot above. For dry runs, F_{max} did not exceed ~2.9 kN (for many, <1 kN), whereas IFCI run peak values reached ~5.8 kN (Extended Data Fig. 2). In dry runs, F_{max} correlates with P_{max}, because driving pressure is their only energy source for deformation and stress-induced fragmentation. In contrast, most of the IFCI runs reveal the anticipated thermohydraulic boost, which added significantly more energy (and thus also entropy) into the process of fragmentation, producing also a considerably larger deviation of data points from the diagonal in the upper IFCI field compared with those in the dry regime (Fig. 3a). We infer that the three outlier IFCI runs (IFCI01, IFCI03 and IFCI09), which plot among the dry runs, did not experience significant interaction of magma with coolant, despite having equivalent initial conditions. This suggests that the IFCI energy yield is sensitive to subtle dynamic controls at laboratory (decimetre) scale. We tested different melt masses (thickness of melt plug), and they had no substantial influence on explosivity, nor on the likelihood of achieving efficient IFCI runs.

The increase in the fragmentation efficiency with IFCI is also reflected in particle grain sizes. Sieve data for particles ≤2 mm ('ash') from seven dry runs and five IFCI runs show increased IFCI fragmentation. On average, IFCI runs generated 2.25 times the mass of ash particles compared with dry runs (Extended Data Fig. 3). Particularly interesting is the increase in fine ash (<125 µm)—this matches the bulk of seafloor ash discovered at Havre[4], and is not a particle population that is predicted as significant for submarine volcanism[7]. The proportion of fine ash with IFCI is ~240% of that produced in dry runs (14.1% versus 5.8%; Fig. 3c).

Identifying IFCI's morphometric fingerprint at Havre

Curviplanar Havre ash grains do not share the morphology of ground-sampled particles from dry runs (DG) or open IFCI runs (without U-tube, IG) (Fig. 4). We infer that ground-sampled

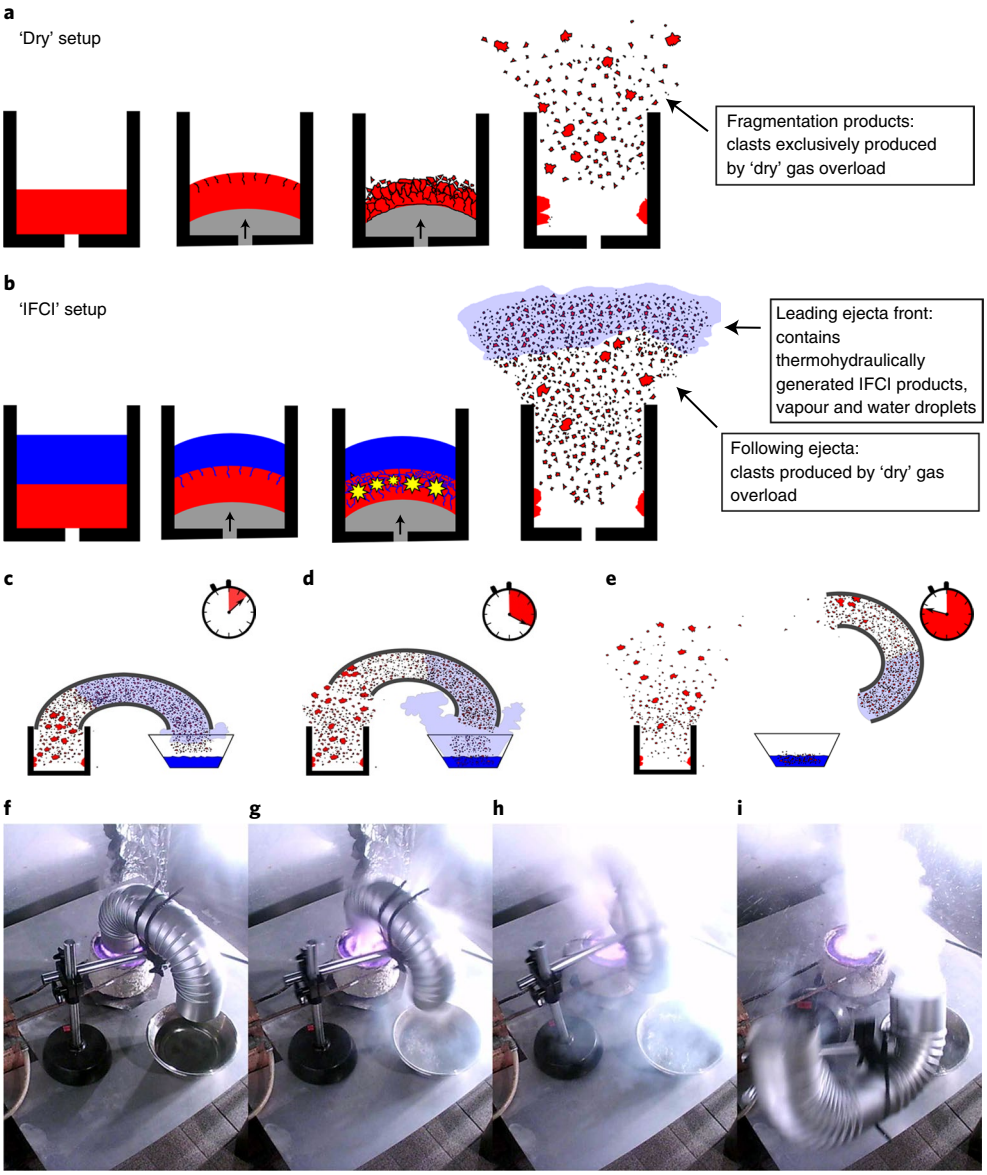

Fig. 2 | Melt fragmentation experiments. a, Dry runs: the melt plug (red) was deformed by injecting gas, causing stress-induced brittle fragmentation. **b**, IFCI runs: seconds before gas injection, water was added atop the plug; subsequently, intruding cracks opened when gas deformed the plug, initiating downward-advancing IFCI that thermohydraulically 'boosted' fragmentation. IFCI particles are most abundant in the leading ejecta front. **c**–**e**, U-tube experiments: the fine particles from the leading ejecta front were collected in a water bowl via a U-shaped tube (**c**). Following, coarser ejecta particles enter the tube shortly after (**d**), then impact momentum causes the tube to detach and move away from the crucible (**e**), with very few particles deposited into the bowl. **f**–**i**, Images: before the run (**f**), and at 33 ms (**g**), 67 ms (**h**) and 167 ms (**i**) after initiation of fragmentation (see also Supplementary Video 1).

particles from IFCI runs are a mixture of dry-formed and thermohydraulically fragmented grains, with population differences in shape that place them apart from the other samples.

U-tube and wall-sampled particles from IFCI runs show, unlike ground-sampled ones, clear similarities to natural ash samples (Nat1–Nat6), as verified by *t*-tests and *e* (quivalence)-tests for all 23 shape parameters. Scanning electron microscopy (SEM) imagery and high-resolution X-ray microtomography show that these grains share surface features such as steps (Fig. 4). IU samples contain predominantly grains from the leading ejecta front generated by IFCI, and IW samples show no significant differences from IU ones in any tested shape parameter. Twelve parameters are verified as significantly similar according to *e*-tests (other shape parameters had large variance differences that precluded meaningful *e*-tests), indicating high similarity. This suggests that IW samples originated, like IU samples, from the leading ejecta front, and that in our experiments IFCI processes generated particles with a characteristic morphometric 'fingerprint'. This fingerprint is shared by Havre's curviplanar natural grains, which are dominant in Havre's seafloor deposits of fine to extremely fine, 3–8 phi, ash[4]. We therefore infer that IFCI played the major role in generating Havre's ash.

Deep-sea conditions favour IFCI

The ratio of thermohydraulic to dry-generated grains in open IFCI experiments is measurably lower than in the main Havre ash deposits, in which curviplanar particles are dominant[4]. IFCI processes at Havre were thus apparently more efficient than in the laboratory.

One of the biggest differences between laboratory conditions versus those at Havre is the much higher ambient pressure in the

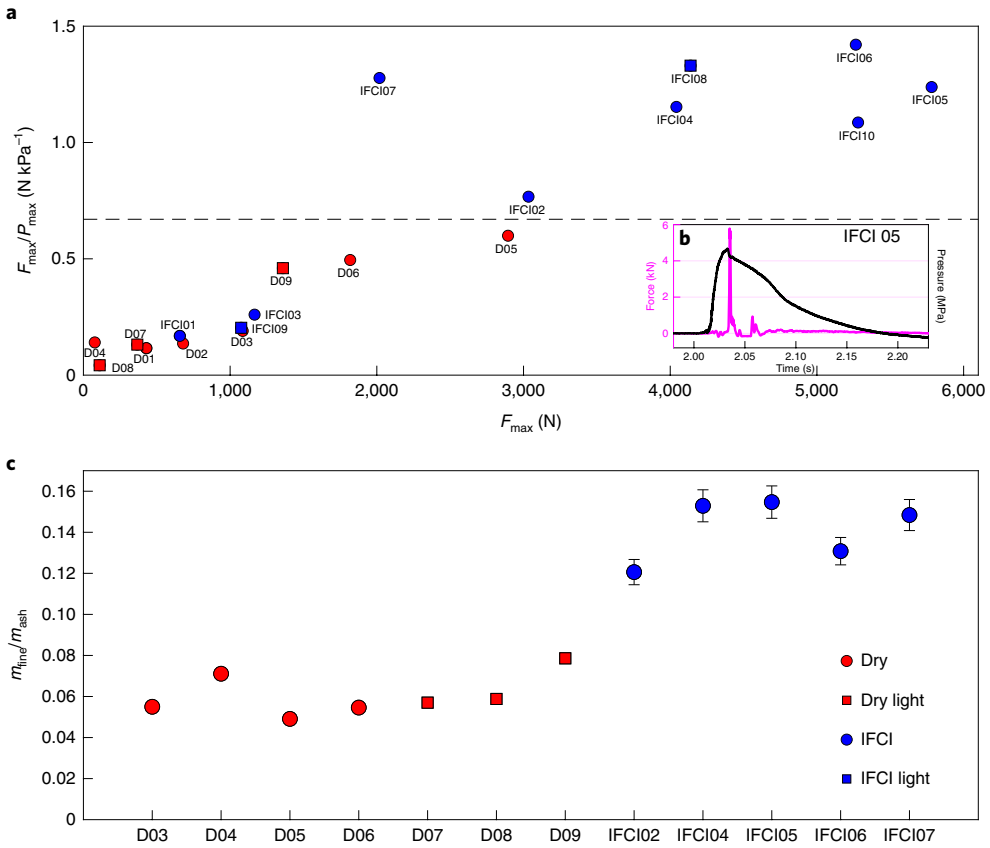

Fig. 3 | Increased explosivity in IFCI fragmentation experiments. a, Recoil-force peaks F_{max} normalized over maximum driving pressure P_{max} and plotted over themselves for dry (D) and IFCI runs. The squares indicate experiments with reduced melt mass. The dashed line indicates the empirical boundary between two regimes. Dry runs plot below the line, whereas most IFCI runs plot above it, reflecting the additional thermohydraulic fragmentation boost. IFCI runs of low efficiency plot together with dry runs. **b**, An example showing the pressure (black) and force (magenta) signals for an IFCI run plotted over time (range 250 ms). **c**, Mass ratio of fine ash (<125 μm) over total ash mass. Error bars indicate measurement uncertainties and are displayed where larger than the marker.

latter (0.1 versus ~10 MPa). A mechanical consequence of a higher confining pressure is stronger driving of water into opening cracks, and this water ingress, as well as an initial magmatic expansion that opens them, are necessary to initiate IFCI. Two thermodynamic factors most strongly control the efficiency of IFCI: heat transfer rates from melt to water (controlling energy available for thermohydraulic conversion) and expansion rates of water that acts as a 'wedge' inside the crack (controlling how effectively this energy is converted into mechanical work).

Our laboratory heat transfer rates were mediated by vapour almost instantaneously generated when water contacted melt (Leidenfrost effect[21,24]). Unlike for MFCI[18,21,25], no stable vapour film is required for IFCI; instead, vapour films inhibit IFCI because they prevent efficient heat transfer from melt to water. Shock waves are generated the moment pressurized gas hits the ceramic barrier and overlying melt, and cause the vapour film to collapse[21,23,26]. We cannot be sure, however, that there is no re-formation, even locally, of a vapour film by the time of crack opening.

Under laboratory conditions, 30% of IFCI runs with water flooding did not produce recognizable IFCI fragmentation according to Fig. 3a. We infer that these intended IFCI runs 'failed' because the required precondition—synchronous crack opening and water invasion (Fig. 1)—was not met, possibly because local film boiling inhibited interaction. This finding suggests that IFCI requires a critical density of simultaneous cracking with direct water–melt contact.

With increasing water depth and pressure, vapour ceases to impede IFCI, and this happens at pressures much lower than critical for sea water (~30 MPa)[16]. The key process, stable film boiling, is strongly suppressed from 1 MPa, and at 10 MPa (~1 km b.s.l.) meta-stable film boiling becomes impossible[16]. Consequently, IFCI is favoured in a deep-sea environment, compared with shallower settings with lower ambient pressure.

With no vapour film, water directly contacts melt, and heat transfer rates are controlled by conduction and convection. Experiments have found that the efficiency of heat transfer between hot rock and water flowing into cracks is increased under increased pressures[27].

Higher pressures also enhance the rate of water expansion. Figure 5 compares the evolution of the thermal expansion coefficient β with temperature, computed for water under laboratory and seafloor pressure conditions. In addition, values for sea water at 1 km depth are plotted, based on measurements under oceanic temperatures[28]. At low water temperatures, β is slightly larger for pure water under high pressure conditions (for example, 1.8 °C^{-1} versus 1.6 °C^{-1} at 30 °C). This difference is more pronounced for the measurements of seawater at high pressure (for example, 2.4 °C^{-1} at 30 °C, which is 48% larger than β for pure water at 0.1 MPa). The dominant factor controlling β is, however, the water temperature (Extended Data Fig. 4). At a water temperature of 100 °C, β is 4.5 °C^{-1}. At 310 °C, β is more than three times as large (14.8 °C^{-1}), so the same amount of heat transferred would therefore result in significantly larger expansion rates, and considerably enhance the efficiency of IFCI.

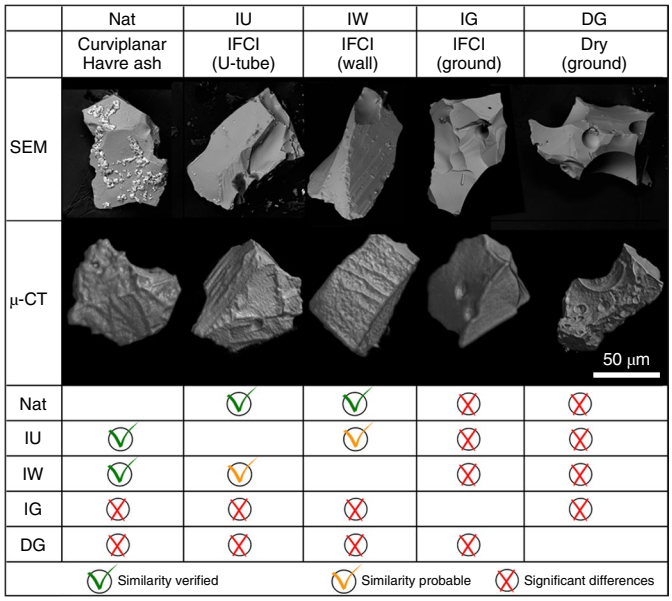

Fig. 4 | Morphometric analysis results by *t*-tests and *e*-tests. Typical particles imaged with SEM and μ-CT (image pixel size 0.56 μm). Natural ash ('Nat') is significantly similar to particles from the leading ejecta front of IFCI experiments (IU and IW), which are highly similar to one another.

In contrast to water at atmospheric pressure (boiling point ~100 °C), water at 10 MPa does not vaporize below ~311 °C and can therefore exploit the full range of IFCI intensification. Thermodynamically, IFCI processes should thus be more efficient under deep submarine conditions than in the laboratory.

'Explosive' ash generation under unexpected conditions

IFCI is an unusual explosive process. This thermohydraulic non-equilibrium mechanism generates fine ash at extreme rates by converting heat into intense mechanical work. It is based on an inherently accelerating feedback mechanism fed by increases in both contact surface and heat transfer rates, leading to rapid and accelerating expansion on microsecond timescales, an explosive rate. However, unlike MFCI, at deep seafloor conditions (or similar ones beneath thick glaciers), no dramatic steam expansion would follow the hydraulic stage. Although considerable kinetic energy release can be expected (based on the observed surplus of F_{max} in the IFCI experiments), the higher mass density and viscosity of water compared with air in subaerial volcanic settings would cause significantly reduced ejection speeds for ash particles. Instead, newly generated fine ash particles would be primarily transported by convective movements of the heated ocean water. Their small settling velocities enable widespread dispersion, but explosive expansion has been effectively suppressed.

A study of Havre pumice concluded that the pumice-raft-generating phase was not driven by magmatic explosions[3]. However, an ~70-km-long subaerial vapour plume was observed above the eruptive centre of Havre[1], which is evidence for high rates of heat and energy transfer during one observed stage of the Havre eruption. Furthermore, a concomitant bluish semi-opaque plume at the ocean surface, offset from the pumice raft[1], indicates that fine particles (ash) were scattering light down-current from the thermal source of the vapour plume. Fine ash of the main event comprises mostly curviplanar particles[4], which morphologically match our experimentally generated IFCI particles. We infer that, at some point(s) during the main phase of the eruption, ash production and heat transfer rates at Havre were increased by IFCI processes, and that IFCI was the mechanism that fuelled ash transport towards the surface in a strengthened convective plume.

The presence of fluidal ash particles in the same deposits implies that, in Havre's main phase, inhomogeneous magma was erupted and fragmented by multiple processes[4]. This is consistent with our findings that suggest that the thermohydraulic boost of IFCI was superimposed on rapid and extensive, magmatically driven, fragmentation, which might have occurred either simultaneously or in alternation with other processes during the pumice-raft-generating phase.

We conclude that IFCI can operate in all deep-sea eruptive settings. Because its major requirement is initial magmatic cracking, we suggest that it can operate with all magmatic compositions. The primary effects of IFCI at depth are intensified fragmentation and heat transfer, but without requiring vapour-driven

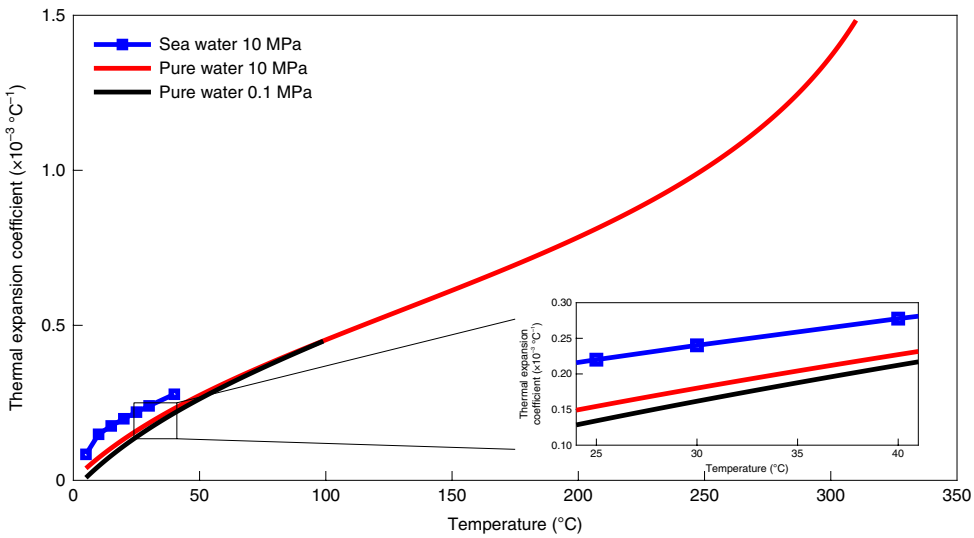

Fig. 5 | Thermal expansion coefficient at laboratory and seafloor pressures. The volumetric thermal expansion coefficient β was computed for water at atmospheric pressure (0.1 MPa; black) and 10 MPa (red). In addition, measured data for saline water (within 0.1% accuracy)[28] are plotted for oceanic temperatures (solid blue lines). Water boils much hotter on the seafloor, allowing higher thermal expansion coefficient values that increase the IFCI efficiency under deep-sea conditions.

particle transport. Deep-sea eruptions in which it is a major process are far more energetic than classic (subaerial) 'effusive' eruptions, resulting in an increased production of fine ash, yet may lack the jets and plumes driven by gas expansion typifying explosive ones. Any process cracking a hot fuel into which a coolant can be driven invites IFCI—its fingerprint can be detected through morphometric analysis of the resulting small particles. Beyond submarine volcanoes, IFCI is insensitive to many controls thought to limit explosive magma–water interaction, and it may be expected with hot dry rocks or other hot brittle materials in the deep ocean, as well as with magmatism beneath thick ice on glacier-bearing planets.

Online content

Any methods, additional references, Nature Research reporting summaries, source data, extended data, supplementary information, acknowledgements, peer review information; details of author contributions and competing interests; and statements of data and code availability are available at https://doi.org/10.1038/s41561-020-0603-4.

Received: 6 January 2020; Accepted: 28 May 2020;
Published online: 29 June 2020

References

1. Carey, R. et al. The largest deep-ocean silicic volcanic eruption of the past century. *Sci. Adv.* **4**, e1701121 (2018).
2. Jutzeler, M. et al. On the fate of pumice rafts formed during the 2012 Havre submarine eruption. *Nat. Commun.* **5**, 3660 (2014).
3. Manga, M. et al. The pumice raft-forming 2012 Havre submarine eruption was effusive. *Earth Planet. Sci. Lett.* **489**, 49–58 (2018).
4. Murch, A. P., White, J. D. L. & Carey, R. J. Characteristics and deposit stratigraphy of submarine-erupted silicic ash, Havre Volcano, Kermadec Arc, New Zealand. *Front. Earth Sci.* **7**, 1 (2019).
5. Zimanowski, B., Wohletz, K., Dellino, P. & Büttner, R. The volcanic ash problem. *J. Volcanol. Geotherm. Res.* **122**, 1–5 (2003).
6. Németh, K. & Kósik, S. Review of explosive hydrovolcanism. *Geosciences* **10**, 44 (2020).
7. Cas, R. A. F. & Simmons, J. M. Why deep-water eruptions are so different from subaerial eruptions. *Front. Earth Sci.* **6**, 198 (2018).
8. Zimanowski, B. & Büttner, R. in *Geophysical Monograph Series* (eds White, J. D. L. et al.) 51–60 (American Geophysical Union, 2003).
9. Wohletz, K. H. in *Explosive Subaqueous Volcanism* (eds White, J. D. L. et al.) 25–49 (American Geophysical Union, 2003).
10. McBirney, A. R. Factors governing the nature of submarine volcanism. *Bull. Volcanol.* **26**, 455–469 (1963).
11. Board, S. J., Hall, R. W. & Hall, R. S. Detonation of fuel coolant explosions. *Nature* **254**, 319–321 (1975).
12. Kokelaar, P. Magma–water interactions in subaqueous and emergent basaltic. *Bull. Volcanol.* **48**, 275–289 (1986).
13. Wohletz, K. H. Explosive magma–water interactions: thermodynamics, explosion mechanisms, and field studies. *Bull. Volcanol.* **48**, 245–264 (1986).
14. Zimanowski, B., Büttner, R., Lorenz, V. & Häfele, H.-G. Fragmentation of basaltic melt in the course of explosive volcanism. *J. Geophys. Res. Solid Earth* **102**, 803–814 (1997).
15. Berthoud, G. Vapor explosions. *Annu. Rev. Fluid Mech.* **32**, 573–611 (2000).
16. Wohletz, K. H., Zimanowski, B. & Büttner, R. in *Modeling Volcanic Processes: The Physics and Mathematics of Volcanism* (eds Fagents, S. A. et al.) 230–257 (Cambridge University Press, 2013).
17. White, J. D. L., Schipper, C. I. & Kano, K. in *The Encyclopedia of Volcanoes* 2nd edn (ed. Sigurdsson, H.) 553–569 (Academic Press, 2015).
18. Moitra, P., Sonder, I. & Valentine, G. A. Effects of size and temperature-dependent thermal conductivity on the cooling of pyroclasts in air. *Geochem. Geophys. Geosyst.* **19**, 3623–3636 (2018).
19. Büttner, R., Dellino, P., La Volpe, L., Lorenz, V. & Zimanowski, B. Thermohydraulic explosions in phreatomagmatic eruptions as evidenced by the comparison between pyroclasts and products from molten fuel coolant interaction experiments. *J. Geophys. Res. Solid Earth* **107**, 2277 (2002).
20. Schipper, C. I. & White, J. D. L. Magma–slurry interaction in Surtseyan eruptions. *Geology* **44**, 195–198 (2016).
21. Büttner, R. & Zimanowski, B. Physics of thermohydraulic explosions. *Phys. Rev. E* **57**, 5726–5729 (1998).
22. Zimanowski, B., Büttner, R., Dellino, P., White, J. D. L. & Wohletz, K. H. in *The Encyclopedia of Volcanoes* (eds Sigurdsson, H. et al.) 473–484 (Elsevier, 2015).
23. Austin-Erickson, A., Büttner, R., Dellino, P., Ort, M. H. & Zimanowski, B. Phreatomagmatic explosions of rhyolitic magma: experimental and field evidence. *J. Geophys. Res.* **113**, B11201 (2008).
24. Zimanowski, B., Fröhlich, G. & Lorenz, V. Quantitative experiments on phreatomagmatic explosions. *J. Volcanol. Geotherm. Res.* **48**, 341–358 (1991).
25. Schipper, C. I. et al. Vapour dynamics during magma–water interaction experiments: hydromagmatic origins of submarine volcaniclastic particles (limu o Pele). *Geophys. J. Int.* **192**, 1109–1115 (2013).
26. Büttner, R., Dellino, P., Raue, H., Sonder, I. & Zimanowski, B. Stress-induced brittle fragmentation of magmatic melts: theory and experiments. *J. Geophys. Res. Solid Earth* **111**, B08204 (2006).
27. Ma, Y., Zhang, Y., Huang, Y., Zhang, Y. & Hu, Z. Experimental study on flow and heat transfer characteristics of water flowing through a rock fracture induced by hydraulic fracturing for an enhanced geothermal system. *Appl. Therm. Eng.* **154**, 433–441 (2019).
28. Bradshaw, A. & Schleicher, K. E. Direct measurement of thermal expansion of sea water under pressure. *Deep Sea Res. Oceanogr. Abstr.* **17**, 691–706 (1970).

Methods

Fragmentation experiments. For each run, crushed rock of mass m_{melt} was inductively heated under non-equilibrium conditions in a 10-cm-diameter cylindrical steel crucible. Standard runs used 250 g of rock; 'light' experiments used a reduced m_{melt} of 100 g. Within an 80 min period, the crushed dome rock material was heated up to a temperature of 1,573 K then equilibrated for 30 min. It was then cooled over a 30 min period to the experimental temperature of 1,423 K. Throughout this process, the crucible was covered by a steel lid, which did not contact the melt and which was removed only seconds before the experiment. The heating procedure was found to provide homogeneous melt temperatures (within a range of 2 K) in calibration experiments in which this parameter was measured at different times, depths and locations using a type S thermocouple.

'Dry run' routines were based on standard experiments for determining material-specific fragmentation and kinetic energy release rates and used that standard setup[26,29] (Extended Data Fig. 5).

In preparation for each run, a steel-reinforced rubber hose 8 m long with 8 mm (inner) diameter, leading from an argon gas reservoir to a closed high-speed solenoid valve, was pressurized. At a pressure of 8.5 MPa, the valve of the gas reservoir was closed. The inner volume of the hose hence represents the driving volume of the pressurized gas. A pipe connected the solenoid with the gas inlet into the crucible, which was covered by a ceramic barrier (diaphragm) placed, without bonding, to block rock fragments or melt from entering the gas inlet. With initiation of the experiment, the high-speed solenoid was opened, and the pressurized argon was injected from below into the cylindrical plug of melt.

When rapidly deformed by the expanding injected gas, a silicate melt behaves brittlely[23,26,29,30]. Like a glass pane hit by a football, the plug deformed until the critical shear stress was reached, at which point it broke, with elastically stored energy converted into fragmentation and kinetic energy[26,29,30]. In the setup geometry used, melt fragmentation is initiated by cracks opening at the top and subsequently progressing downwards[23,26].

The pressure of the driving gas was measured by a Kistler 603B pressure transducer (Extended Data Fig. 5). A Kistler 9031A force transducer measured the vertical component of the repulsion force exerted on the crucible, herein termed the 'recoil force'. Force and pressure signals were measured at a sampling rate of 100 kHz.

The heating procedure, geometry, and sensor setup for IFCI runs were the same as for dry runs, but we added a hosepipe leading to the top of the crucible. Two seconds before the gas valve opened, 240 ml of deionized water flooded the crucible, forming a water layer atop the melt. This produced no force signal, audible cracking, or fragmentation visible on high-speed video. Only when injected gas initiated deformation and fragmentation did water intrude into the opening cracks and produce IFCI.

To separately sample leading ejecta, mostly from IFCI, we modified some runs with a U-shaped 10-cm-diameter steel tube mounted such that one opening was a few centimetres above the crucible orifice (Fig. 2). The other end led to a 600 ml bowl of deionized water. In these U-tube runs, small particles (plus water and steam) of the leading ejecta front were guided into the water bowl. The tube remained fixed until larger fragments of the following ejecta entered it (~30 ms after fragmentation began), pushing the U-tube upward and removing it from the particle ejection path (Fig. 2c–e and Supplementary Video 1). Fragments ejected after U-tube separation followed free ballistic trajectories and were deposited across the whole experimental area ('ground'). U-tube separation ensured that most fragments in the water bowl were from the leading ejecta front.

Analysis of force and pressure signals. Force and pressure signals, their temporal development and the relation between them carry information about how the melt plug is accelerated and fragmented[23,26,29].

Technically, for all fragmentation experiments, the same initial gas expansion energy was provided as input. However, due to the stochastic nature of material failure processes and crack paths[31], the times when fragmentation is completed and when the gas jet breaks through differed between each run. Thus, the actual gas-driven energy input before breakthrough varied. We used the maximum driving pressure P_{max} as an indicator for this effective expansion work. This energy causes plastic deformation and is (mainly) stored as elastic energy, which then drives the fragmentation and is released as kinetic energy of the ejecta[26,29].

In this study, we used the maximum recoil force F_{max} exerted on the crucible as a measure for the mechanical response of the plug towards the gas expansion with pressure P_{max}.

While for dry runs we would expect F_{max} to be correlated with P_{max}, in the case of IFCI runs, rapid thermohydraulic expansion has to be considered as an additional source of mechanical energy.

Particle sampling. Before each run, the experimental area was thoroughly cleaned to avoid any contamination. Particles generated by the fragmentation experiments were collected after each run, using three different methods:

- Ballistically transported particles deposited on the table and floor (DG and IG, for notation see Extended Data Fig. 1a) were retrieved using a vacuum cleaner with microporous paper bags.
- Particles generated in open IFCI runs, which were deposited in water droplets on the ceiling and walls (IW, see Extended Data Fig. 1b), were collected using paper tissues, which were subsequently dried.
- Particles collected in U-tube runs in the water bowl (IU) were retrieved by using paper filters and subsequently dried.

We note that it was not possible to avoid particle loss in any of the configurations. In particular, it is expected that not all of the fine IU and IW particles collected could be retrieved from the paper tissues and filters. Therefore, the sieving curves of IFCI particles are biased towards larger grains. The bias is probably not large, given the very low per-particle mass of the fine ash-grade particles.

Glassy vesicular Havre ash grains fit three subclasses: curviplanar, angular and fluidal[4]. The experimental grains of the 4 phi (>64 μm and <125 μm) sieve fraction were compared with ash particles of the same size from six Havre seafloor sites: Nat1 to Nat6 (Extended Data Fig. 1c). We exclusively focused on the curviplanar grains dominant in Havre ash samples, which can be attributed to the main eruptive phase (layers S1 and S2)[4].

Grain size analysis. All particles collected were sieved at 1 phi intervals down to a grain size of 4 phi (64–125 μm), with the smallest particles accumulating in the pan. One of the characteristics of fuel–coolant interaction processes is the increased production of fine ash grains. To check whether this effect is also measurable for IFCI on Havre material, the two finest fractions, 4 phi (125 μm to 64 μm) and smaller than 4 phi (<64 μm), were binned, and their mass m_{fine} relative to the total amount of 'ash' m_{ash}, that is, the mass of particles smaller than −1 phi (<2 mm), was determined as a ratio. We estimate the accuracies for m_{ash} and m_{fine} to be within 1% and 5%, respectively. According to propagation of error, the ratio m_{fine}/m_{ash} therefore has an estimated uncertainty of 5.1%.

Morphometric analysis. For morphometric analysis, a population of 4 phi particles was randomly selected and mounted on carbon-coated tape, ensuring that the grains did not touch one another. Backscatter electron scans were produced with a resolution of 2,048 × 1,536 pixels, using a Zeiss Sigma VP FEG scanning electron microscope. The image of each particle was next isolated and binarized, resulting in a black-and-white image showing its silhouette, that is, the projection of the particle onto an underlying plane. These binarized images were used as input data for the particle shape analyser software PARTISAN[32]. This program was developed to quantify shapes of particle outlines, based on 5 morphometric systems[33–37], and computes 23 dimensionless shape descriptors (of which several are redundantly used in different systems, sometimes with different labels/names). The shape parameters and references to their computation are listed in Extended Data Fig. 6.

Each dataset was tabulated, then tested pairwise, for example A–B, A–C, A–D, B–C, B–D and C–D, by applying a sequence of statistical tests, following a test procedure presented in an earlier study[38] (Extended Data Fig. 7). All tests were performed with the software IBM SPSS Statistics 26, selecting a level of significance α of 5%.

First, a Levene test[39] was used to determine whether the variances between compared datasets were homogeneous or not. As a second step, two-tailed pooled variance *t*-tests[38,39] or separated variance *t*-tests[40] were used. We identified parameters that indicated significant differences, without corrections[41], and thereby determined types of experiments that reproduced grains with features most similar to the natural Havre ash (sample sizes and results of each test can be downloaded from the PANGAEA depository[42]). This approach minimizes the number of type I errors (indications of differences where there are none).

To verify, for any two datasets that did not show significant differences from one another in *t*-tests, a high degree of similarity, we applied *e*-tests. This method was introduced for image particle analysis with volcanic ash[38] and tests whether the confidence interval *C* of the tested dataset lies within a given range *D*, specified by the threshold D_{max}. For *C*, a range of 5% was used. For mathematical details on this method, the reader is referred to the 2012 study by Dürig et al.[38]. *e*-Tests are based on the pooled Student's *t*-function and thus only provide reliable results for datasets with homogeneous variances. *e*-Test results based on datasets with unequal variances have therefore been omitted and are displayed as '(…)', indicating that no statement about possible equivalence can be made (Extended Data Figs. 8–10).

Ranges of *D* were calibrated to specific shape parameters of Havre ash by applying *e*-tests pairwise to the natural curviplanar ash samples, that is, the samples Nat1 to Nat6.

In these 15 benchmark tests, the threshold values for *D* were increased stepwise, starting from 0.01 with a step size of 0.01, until the test indicated a significant equivalence in the respective shape parameter. Variances must be homogeneous for this test, so not every *e*-test yielded results for each of the tested shape factors. For all the shape parameters, however, at least one valid threshold value for *D* was found. On the basis of the results of these benchmark tests, the largest of the up to 15 *D* values was used as the shape-parameter-specific threshold D_{max} for testing the experimental grains (Extended Data Fig. 6). D_{max} can thus be seen as a quantity which specifies the 'natural variation' of the respective parameter. We note that, in this approach, it is implicitly assumed that these datasets originate

from the same particle population, which implies that the curviplanar ash particles in Nat1–Nat6 were generated in the same event.

X-ray microtomography. For each sample suite, the 3D external morphology of about 30 particles of the grain fraction between 125 and 64 µm was determined by X-ray microtomography (µ-CT) using a Bruker Skyscan 1172 high-resolution µ-CT scanner. Particles were cleaned in an ultrasonic bath and mounted on a graphite rod holder using vinyl glue. Particles were scanned with a pixel size of 0.54 µm, an X-ray voltage of 34 kV, an X-ray current of 210 µA, a rotation step of 0.46°, with no filter and a frame averaging over 5 scans. Bruker's software NRecon was used to reconstruct the µ-CT projection images into two-dimensional cross sections (slices), using a smoothing parameter of 1, a ring artefact correction index of 4 and a beam-hardening correction of 36%. The programs CTAn and CTVox (both by Bruker) were used for particle image segmentation, and for rendering and displaying the 3D objects.

Volumetric temperature expansion. The change in the volume of a unit under changing temperatures can be expressed as

$$\beta = \frac{\mathrm{dV}}{V_0 \mathrm{dT}}$$

where β is the volumetric thermal expansion coefficient, dV is the change in volume, V_0 is the initial volume, and dT is the temperature change. The volumes were computed for pressures between 0.1 and 10 MPa and temperatures from 4 °C to the boiling point, using the MATLAB toolbox X Steam (version 2.5)[43]. The thermal expansion coefficient β was calculated assuming an initial temperature of 4 °C. A plot showing the resulting values for β is provided in Extended Data Fig. 4. The volume changes for sea water with temperature at 10 MPa presented in Fig. 5 are based on experimental measurements for oceanic temperatures[28].

Data availability

Raw data and results of *t*-tests, including *P* values, *t* values and degrees of freedom, are available on the open-access data archive PANGAEA[42] and can be retrieved under https://doi.org/10.1594/PANGAEA.908865. Additional experimental data, including videos, are available from the corresponding author on request. Source data are provided with this paper.

Code availability

MATLAB routines used for data processing and modelling are available from the corresponding author on request. Source data are provided with this paper.

References

29. Dürig, T. et al. A new method for the determination of the specific kinetic energy (SKE) released to pyroclastic particles at magmatic fragmentation: theory and first experimental results. *Bull. Volcanol.* **74**, 895–902 (2012).
30. Dürig, T., Sonder, I., Zimanowski, B., Beyrichen, H. & Büttner, R. Generation of volcanic ash by basaltic volcanism. *J. Geophys. Res. Solid Earth* **117**, B01204 (2012).
31. Dürig, T. & Zimanowski, B. "Breaking news" on the formation of volcanic ash: fracture dynamics in silicate glass. *Earth Planet. Sci. Lett.* **335**, 1–8 (2012).
32. Dürig, T. et al. PARTIcle Shape ANalyzer PARTISAN – an open source tool for multi-standard two-dimensional particle morphometry analysis. *Ann. Geophys.* **61**, VO671 (2018).
33. Dellino, P. & La Volpe, L. Image processing analysis in reconstructing fragmentation and transportation mechanisms of pyroclastic deposits. The case of Monte Pilato-Rocche Rosse eruptions, Lipari (Aeolian Islands, Italy). *J. Volcanol. Geotherm. Res.* **71**, 13–29 (1996).
34. Cioni, R. et al. Insights into the dynamics and evolution of the 2010 Eyjafjallajökull summit eruption (Iceland) provided by volcanic ash textures. *Earth Planet. Sci. Lett.* **394**, 111–123 (2014).
35. Leibrandt, S. & Le Pennec, J.-L. Towards fast and routine analyses of volcanic ash morphometry for eruption surveillance applications. *J. Volcanol. Geotherm. Res.* **297**, 11–27 (2015).
36. Liu, E. J., Cashman, K. V. & Rust, A. C. Optimising shape analysis to quantify volcanic ash morphology. *GeoResJ* **8**, 14–30 (2015).
37. Schmith, J., Höskuldsson, Á. & Holm, P. M. Grain shape of basaltic ash populations: implications for fragmentation. *Bull. Volcanol.* **79**, 1–16 (2017).
38. Dürig, T., Mele, D., Dellino, P. & Zimanowski, B. Comparative analyses of glass fragments from brittle fracture experiments and volcanic ash particles. *Bull. Volcanol.* **74**, 691–704 (2012).
39. Brosius, F. *SPSS 8 Professionelle Statistik unter Windows* (mitp-Verlag, 1998).
40. Welch, B. L. The generalization of 'Student's' problem when several different population variances are involved. *Biometrika* **34**, 28–35 (1947).
41. Perneger, T. V. What's wrong with Bonferroni adjustments. *BMJ* **316**, 1236–1238 (1998).
42. Dürig, T. et al. Fragmentation experiments with Havre melt: dry and induced fuel-coolant interaction runs. *PANGAEA* https://doi.org/10.1594/PANGAEA.908865 (2019).
43. Holmgren, M. X Steam, Thermodynamic properties of water and steam. *MATLAB Central File Exchange*. https://go.nature.com/3hxTRbh (accessed 21 April 2020).

Acknowledgements

L. Schmid, R. J. M. Baxter and D. Longridge are acknowledged for assisting with particle analysis. We thank I. Schipper for proof-reading and gratefully acknowledge I. Sonder for helpful comments that substantially improved an earlier version of the manuscript. This study was supported by MARSDEN grant U001616; Havre samples were obtained with NSF funding EAR1447559. R.J.C. was funded by Australian Research Council grants DP110102196 and DE150101190, and by US National Science Foundation grant OCE1357443.

Author contributions

J.D.L.W. designed and supervised the Marsden research project. T.D., J.D.L.W., B.Z., R.B. and A.P.M. conducted the laboratory experiments at Physikalisch Vulkanologisches Labor, University of Würzburg. T.D. and N.S. sampled the experimental particles. T.D. conducted two-dimensional morphometry and statistical analysis of both experimental and natural ash with support from D.M. and P.D. D.M., P.D. and T.D. conducted X-ray microtomography and image reconstruction. L.S.S. computed thermal expansion coefficients. R.J.C. was leader of the NSF cruise and helped formulate the Marsden project. J.D.L.W., R.J.C. and A.P.M. took part in the NSF cruise and collected the dome rock used as starting material for melt fragmentation experiments. R.J.C. and A.P.M. provided Havre ash samples and related metadata, including the bathymetric map. Figures and plots were produced by T.D. and L.S.S. T.D. and J.D.L.W. wrote the manuscript, with contributions from all the authors.

Competing interests

The authors declare no competing interests.

Additional information

Extended data is available for this paper at https://doi.org/10.1038/s41561-020-0603-4.

Supplementary information is available for this paper at https://doi.org/10.1038/s41561-020-0603-4.

Correspondence and requests for materials should be addressed to T.D.

Peer review information Primary Handling Editor: Rebecca Neely.

Reprints and permissions information is available at www.nature.com/reprints.

a

notation	particle type	samples from
Nat1	natural	Havre volcano (curvi-planar grains only)
Nat2	natural	Havre volcano (curvi-planar grains only)
Nat3	natural	Havre volcano (curvi-planar grains only)
Nat4	natural	Havre volcano (curvi-planar grains only)
Nat5	natural	Havre volcano (curvi-planar grains only)
Nat6	natural	Havre volcano (curvi-planar grains only)
DG	experimental	Dry run, retrieved on table and floor
IG	experimental	open IFCI run, retrieved on table and floor
IW	experimental	open IFCI run, retrieved in droplets on walls
IU	experimental	IFCI run with U-tube, sampled in water bowl

b

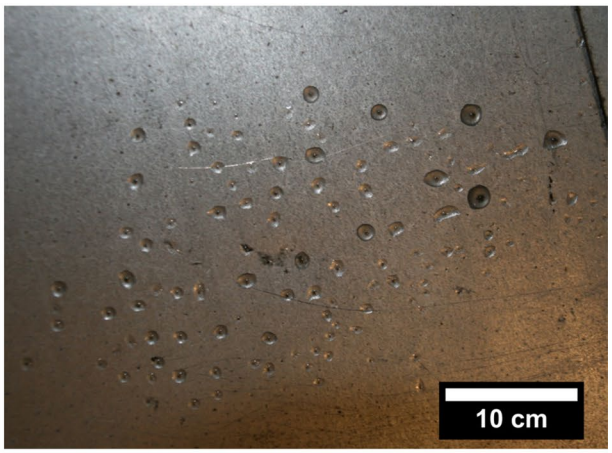

c

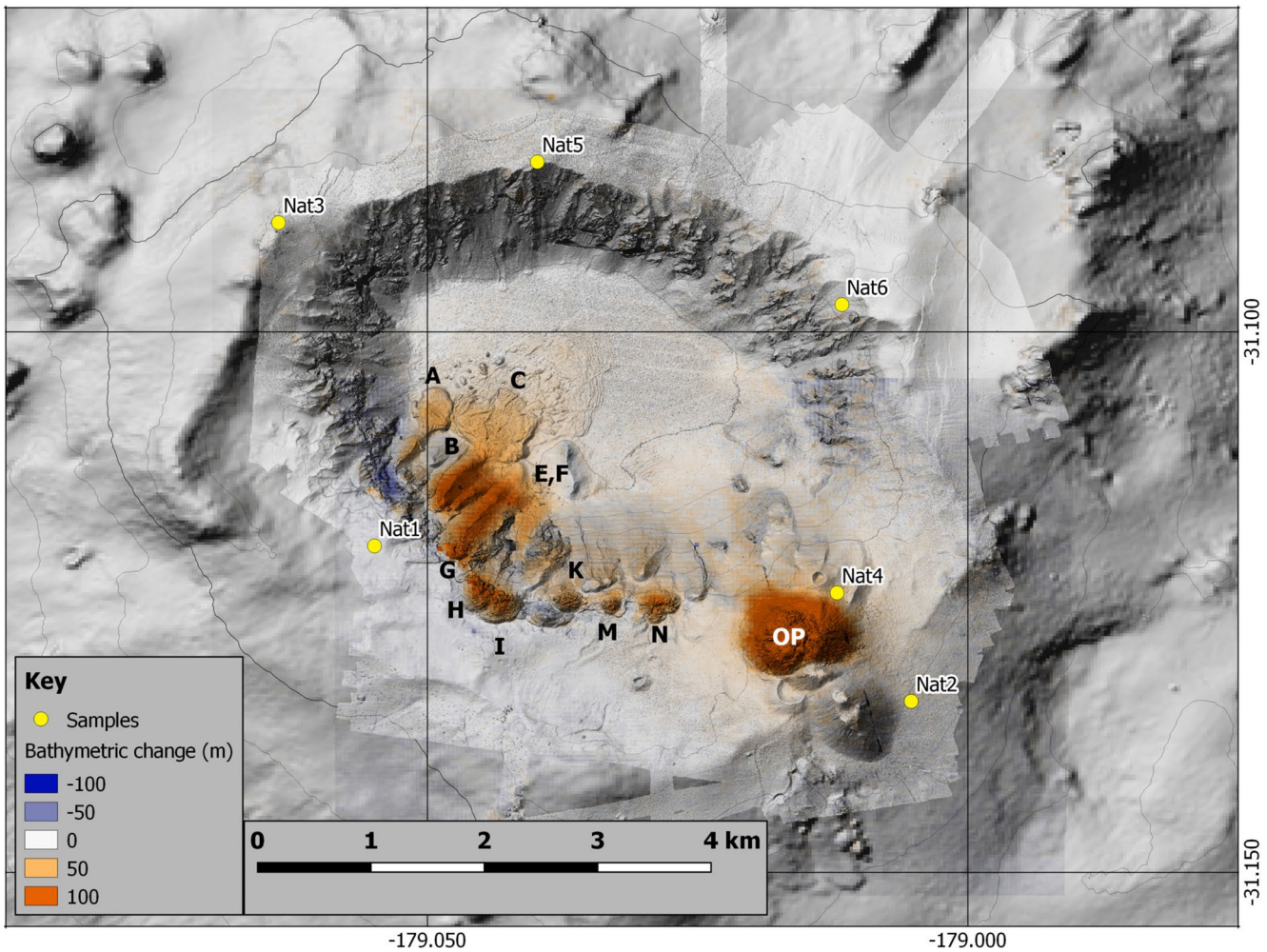

Extended Data Fig. 1 | Notation of studied ash samples and sample locations. a, labels of the ten different particle samples analysed for this study. **b**, photo showing droplets deposited after open IFCI experiments at the ceilings and walls around the experimental area. These droplets contain very fine particles, which are denoted "IW" samples. **c**, map showing vicinity of Havre volcano. It was acquired in 2015 and is adapted from Carey et al.4. Indicated changes can be attributed to the 2012 eruption. Next to pumice and ash, this eruption featured also eleven lava flows, here denoted "A" through "N". The rocks used for the melt experiments presented in this study were collected at the newly formed dome labelled "OP".

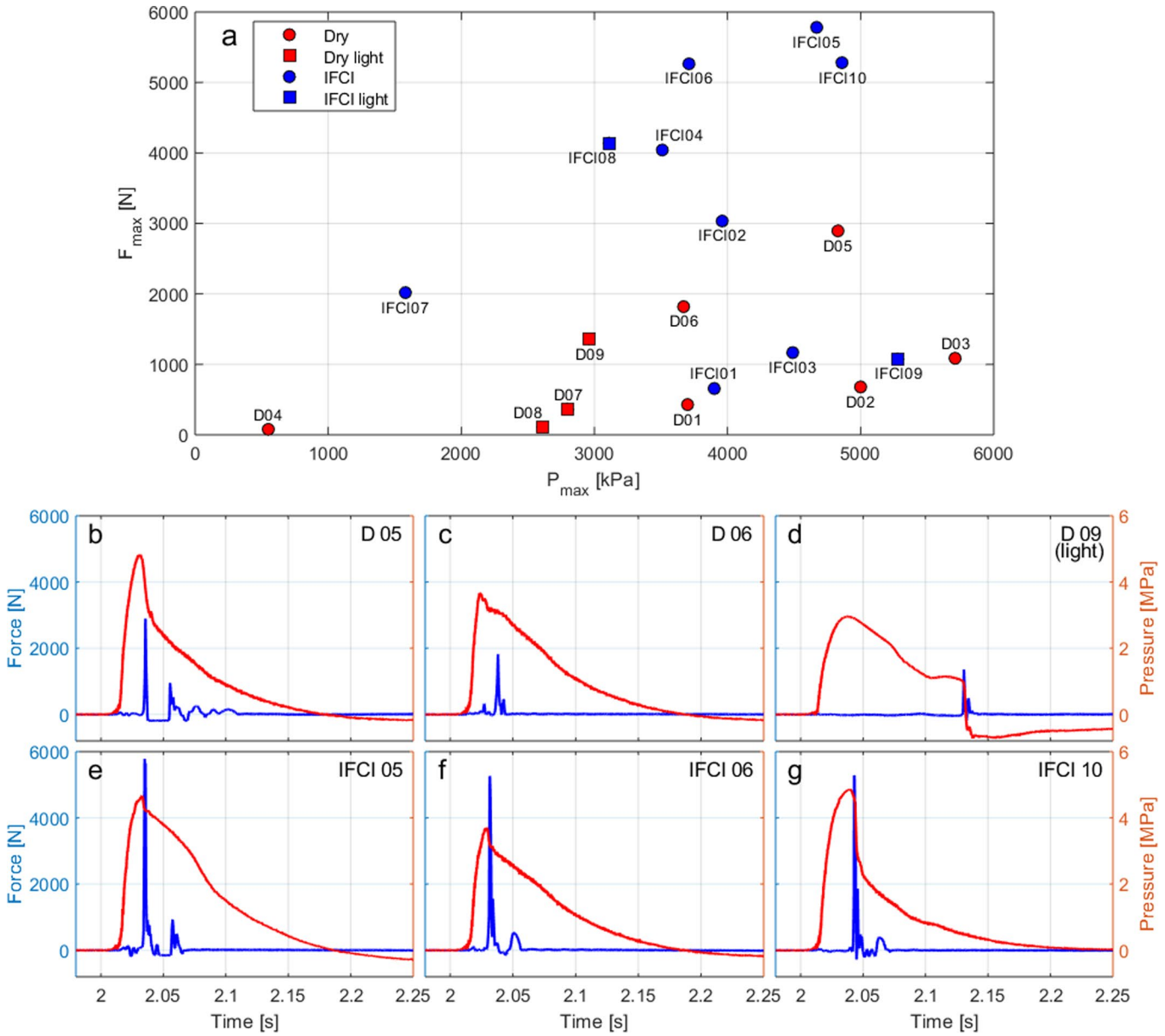

Extended Data Fig. 2 | Recoil-force and driving pressure recorded in fragmentation runs. a, Maximum recoil force Fmax and pressure Pmax measured for dry ("D", red) and IFCI runs (blue). Squares indicate experiments with reduced (100 g) melt mass mmelt. Fmax represents "explosiveness" of response to the initiating driving pressure. Pressure and force curves given for the three strongest dry (**b**-**d**) and IFCI (**e**-**g**) runs. Measurement uncertainties are within marker sizes.

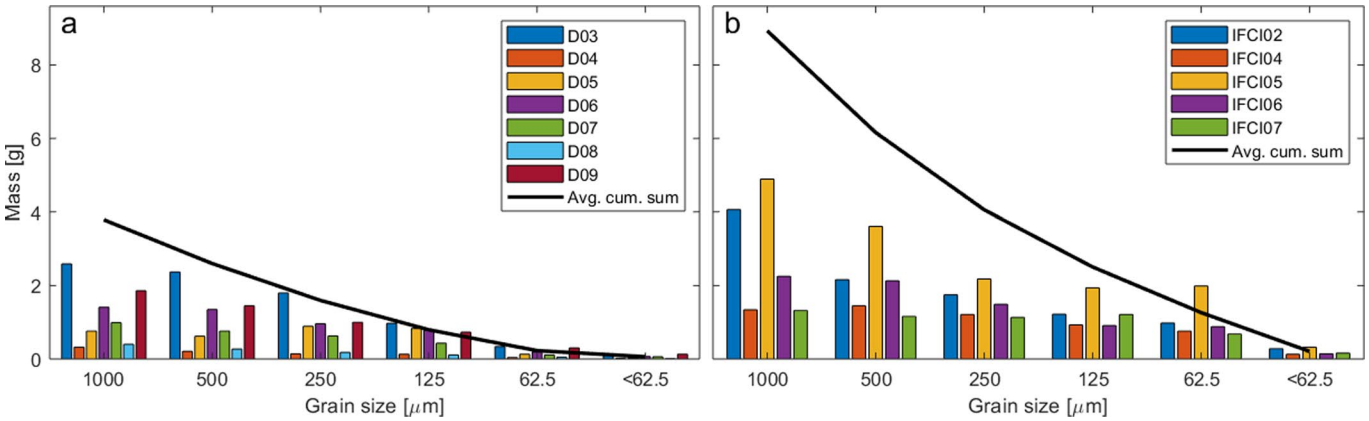

Extended Data Fig. 3 | Grainsize distribution of experimental particles. a, grainsize distributions for seven dry runs and **b**, for five IFCI runs. Black curves for cumulative sums averaged over all samples demonstrate increased amounts of ash generated by IFCI. Notation as in Extended Data Fig. 2.

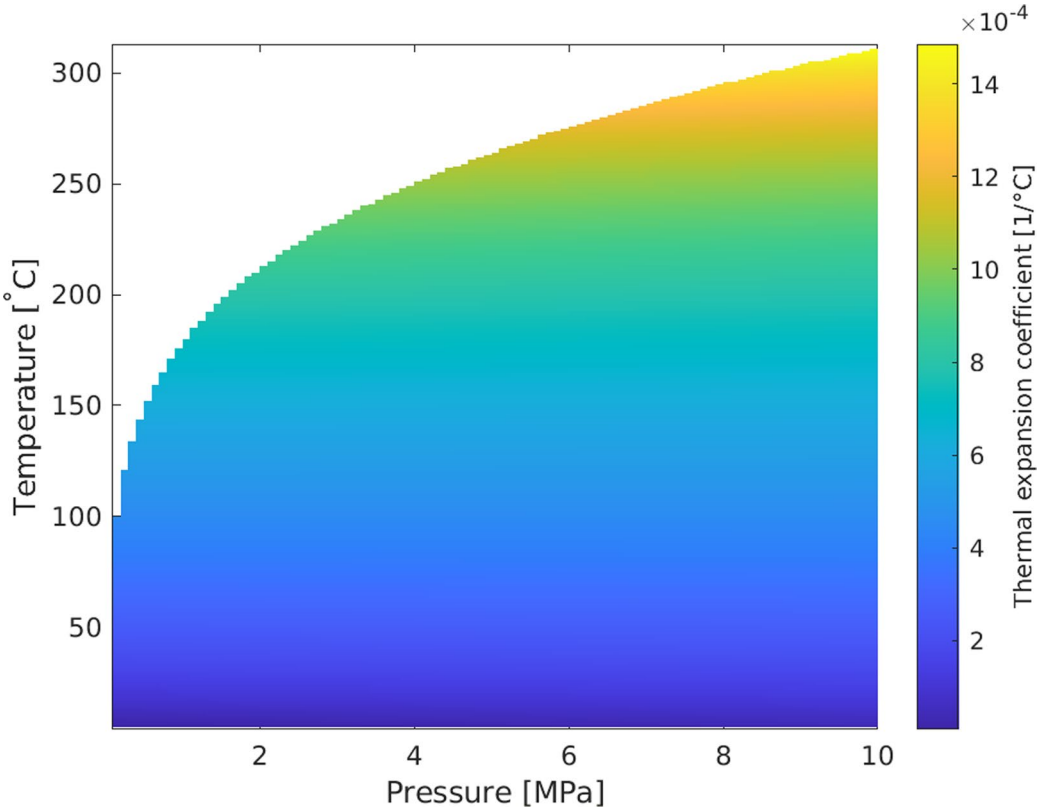

Extended Data Fig. 4 | Thermal expansion coefficient for different pressures. Compared to surface pressure conditions (0.1 MPa), the boiling temperature of water at 1 km depth is significantly higher. This allows the water to reach regimes with considerably higher thermal expansion coefficients. This is one of the reasons why IFCI processes are enhanced under deep-sea conditions.

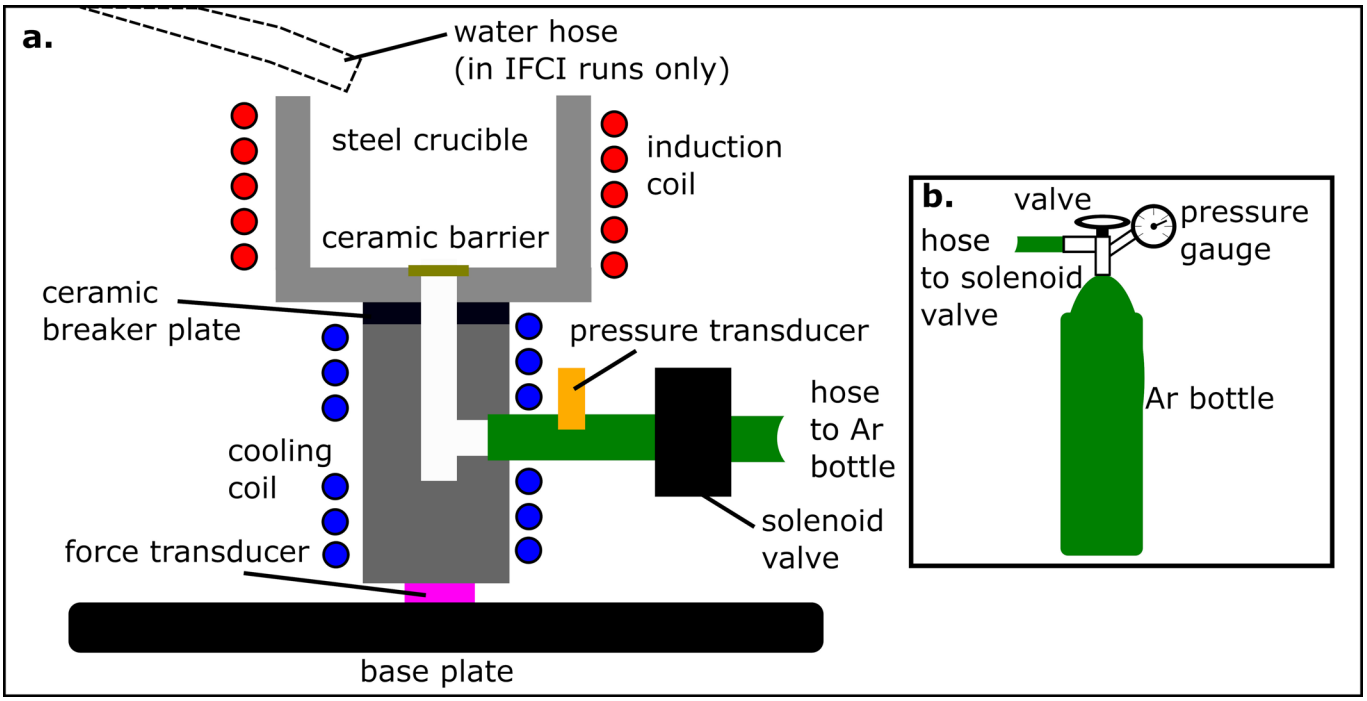

Extended Data Fig. 5 | Schematic setup for dry and IFCI runs. a, cross-section illustrates the configuration of gas inlet and location of sensors. **b**, gas reservoir used to provide the pressurized argon gas for fragmentation experiments.

	notation of shape parameter	D_{max}	morphometric system by
Circ_DL	circularity	0.13	Dellino and La Volpe[30]
Rec_DL	rectangularity	0.07	
Com_DL	compactness	0.06	
Elo_DL	elongation	0.53	
Circ_CI	circularity	0.12	Cioni et al.[31]
AR_CI	aspect ratio	0.45	
Con_CI	convexity	0.07	
Sol_CI	solidity	0.10	
Circ_LL	circularity	0.08	Leibrandt and Le Pennec[32]
Elo_LL	elongation	0.12	
AR_LL	aspect ratio	0.12	
Con_LL	convexity	0.06	
Sol_LL	solidity	0.10	
FF	form factor	0.12	Liu et al.[33]
Con_LI	convexity	0.06	
Sol_LI	solidity	0.10	
AR_LI	aspect ratio	0.14	
Circ_SC	circularity	0.12	Schmith et al.[34]
Rec_SC	rectangularity	0.06	
AR_F	Feret aspect ratio	0.16	
FFa	form factor	0.12	
AR_SC	reciprocal aspect ratio	0.37	
Reg	regularity	0.11	

Extended Data Fig. 6 | Shape parameters and maximum distance ranges D_{max} used for morphometric analyses. The mathematical definitions of the shape parameters can be found in the listed sources. All parameters were computed using the software PARTISAN. Note that some of the shape parameters are used through the various systems, though not always identically named[32].

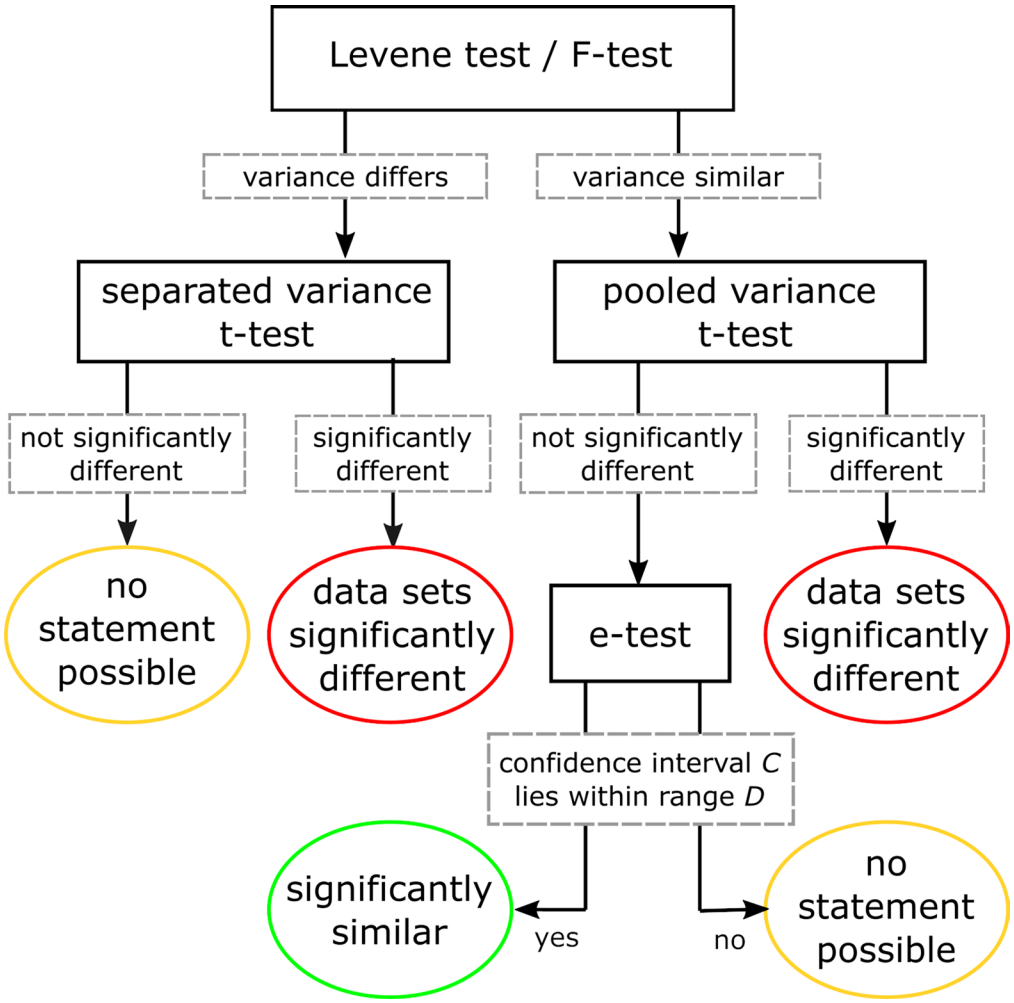

Extended Data Fig. 7 | Statistical testing procedure followed for comparative morphometric analysis. Two samples were first tested for significant differences in their 23 shape parameters, using one of the two t-tests. If variances were comparable, and no significant difference was found in any of the shape parameters, calibrated e-tests were applied to check for significant similarity.

data 1 data 2	IU Nat1	IU Nat2	IU Nat3	IU Nat4	IU Nat5	IU Nat6			
	e-test	e-test	e-test	e-test	e-test	e-test	max. diff.	D_{max}	equivalence verified?
N1	57	57	57	57	57	57			
N2	74	17	28	35	55	38			
Circ_DL	(...)	0.12	0.06	0.06	0.06	0.06	0.12	0.13	yes
Rec_DL	(...)	0.05	0.03	0.03	0.03	0.04	0.05	0.07	yes
Com_DL	(...)	0.06	0.04	0.03	0.03	0.04	0.06	0.06	yes
Elo_DL	(...)	0.42	(...)	(...)	0.24	(...)	0.42	0.53	yes
Circ_CI	0.04	0.10	(...)	0.04	0.05	0.05	0.10	0.12	yes
AR_CI	(...)	(...)	(...)	(...)	0.18	(...)	0.18	0.45	yes
Con_CI	0.03	0.07	0.05	0.04	(...)	0.03	0.07	0.07	yes
Sol_CI	(...)	0.05	0.03	0.03	(...)	(...)	0.05	0.10	yes
Circ_LL	0.03	0.07	0.03	0.03	0.03	0.03	0.07	0.08	yes
Elo_LL	0.06	0.07	(...)	(...)	0.06	(...)	0.07	0.12	yes
AR_LL	0.06	0.07	(...)	(...)	0.06	(...)	0.07	0.12	yes
Con_LL	(...)	0.05	0.04	0.03	0.02	0.03	0.05	0.06	yes
Sol_LL	(...)	0.05	0.03	0.03	(...)	(...)	0.05	0.10	yes
FF	0.04	0.1	(...)	0.04	0.05	0.05	0.05	0.12	yes
AR_LI	0.06	0.08	0.10	(...)	0.07	(...)	0.10	0.14	yes
Con_LI	(...)	0.05	0.04	0.03	0.02	0.03	0.05	0.06	yes
Sol_LI	(...)	0.05	0.03	0.03	(...)	(...)	0.05	0.10	yes
Circ_SC	0.05	(...)	(...)	(...)	0.07	(...)	0.07	0.12	yes
Rec_SC	(...)	0.06	0.04	0.03	0.03	0.04	0.06	0.06	yes
FFa	0.04	0.10	(...)	0.04	0.05	0.05	0.10	0.12	yes
AR_F	0.06	0.09	(...)	0.09	0.09	0.08	0.09	0.16	yes
AR_SC	(...)	0.27	(...)	(...)	0.19	(...)	0.27	0.37	yes
Reg	0.04	0.07	(...)	0.06	0.05	0.05	0.07	0.11	yes

Extended Data Fig. 8 | Results of equivalence tests between sample IU (grains retrieved via U-tube in IFCI runs) and natural ash grains (Nat1–Nat6). Values represent the calculated minimum range *D*, under which the equivalence test would still be passed. The maximum value of *D* for each shape parameter is presented in the column labelled "max. diff.". If this value is equal or smaller than the threshold for curvi-planar ash grains (D_{max}, see also Extended Data Fig. 6), the compared data sets can be treated as significantly similar in the according shape parameter. Equivalence test results are only valid for data sets with homogeneous variances. If this precondition is not fulfilled, results were omitted, denoted by "(...)". None of these values exceed the threshold given by D_{max}, hence it can be concluded that experimental IFCI particles retrieved via U-tube and natural grains show no detectable difference in their shapes.

data 1 data 2	IW Nat1	IW Nat2	IW Nat3	IW Nat4	IW Nat5	IW Nat6			
	e-test	e-test	e-test	e-test	e-test	e-test	max. diff.	D_{max}	equivalence verified?
N1	66	66	66	66	66	66			
N2	74	17	28	35	55	38			
Circ_DL	(...)	0.10	0.07	0.06	(...)	0.07	0.10	0.13	yes
Rec_DL	0.03	(...)	(...)	(...)	0.03	0.03	0.03	0.07	yes
Com_DL	(...)	0.05	0.03	0.03	0.03	0.03	0.05	0.06	yes
Elo_DL	(...)	0.51	0.51	0.45	(...)	0.36	0.51	0.53	yes
Circ_CI	(...)	0.09	0.06	0.06	0.06	0.06	0.09	0.12	yes
AR_CI	(...)	0.32	0.38	0.32	(...)	0.33	0.38	0.45	yes
Con_CI	(...)	(...)	(...)	(...)	0.03	(...)	0.03	0.07	yes
Sol_CI	(...)	0.05	0.02	0.03	0.02	0.02	0.05	0.10	yes
Circ_LL	(...)	0.06	0.04	0.04	0.04	0.04	0.06	0.08	yes
Elo_LL	0.06	0.10	0.11	0.11	0.09	0.10	0.11	0.12	yes
AR_LL	0.06	0.10	0.11	0.11	0.09	0.10	0.11	0.12	yes
Con_LL	0.02	(...)	(...)	(...)	(...)	(...)	0.02	0.06	yes
Sol_LL	(...)	0.05	0.02	0.03	0.02	0.02	0.05	0.10	yes
FF	(...)	0.09	0.06	0.06	0.06	0.06	0.09	0.12	yes
AR_LI	0.05	0.09	0.11	0.10	0.08	0.09	0.11	0.14	yes
Con_LI	0.02	(...)	(...)	(...)	(...)	(...)	0.02	0.06	yes
Sol_LI	(...)	0.05	0.02	0.03	0.02	0.02	0.05	0.10	yes
Circ_SC	0.06	0.07	0.10	0.09	0.08	0.08	0.10	0.12	yes
Rec_SC	(...)	0.05	0.03	0.03	0.03	0.03	0.05	0.06	yes
FFa	(...)	0.09	0.06	0.06	0.06	0.06	0.09	0.12	yes
AR_F	0.06	0.10	0.13	0.11	0.10	0.09	0.13	0.16	yes
AR_SC	0.23	0.32	0.36	0.31	(...)	0.28	0.36	0.37	yes
Reg	(...)	0.07	0.08	0.06	0.06	0.06	0.08	0.11	yes

Extended Data Fig. 9 | Results of equivalence tests between sample IW (grains retrieved after IFCI runs inside water droplets, deposited at ceilings and walls) and natural ash grains (Nat1–Nat6). Values represent the calculated minimum range D, under which the equivalence test would still be passed. The maximum value of *D* for each shape parameter is presented in the column labelled "max. diff.". If this value is equal or smaller than the threshold for curvi-planar ash grains (D_{max}, see also Extended Data Fig. 6), the compared datasets can be treated as significantly similar in the according shape parameter. Equivalence test results are only valid for datasets with homogeneous variances. If this precondition is not fulfilled, results were omitted, denoted by "(...)". None of these values exceed the threshold given by D_{max}, hence it can be concluded that IW particles and natural grains show no detectable difference in their shapes.

data 1	IW		
data 2	IU		
	e-test	D_{max}	equivalence verified?
N1	66		
N2	74		
Circ_DL	0.06	0.13	yes
Rec_DL	(...)	0.07	(...)
Com_DL	0.03	0.06	yes
Elo_DL	0.55	0.53	yes
Circ_CI	0.05	0.12	yes
AR_CI	(...)	0.45	(...)
Con_CI	(...)	0.07	(...)
Sol_CI	(...)	0.10	(...)
Circ_LL	0.03	0.08	yes
Elo_LL	0.07	0.12	yes
AR_LL	0.07	0.12	yes
Con_LL	(...)	0.06	(...)
Sol_LL	(...)	0.10	(...)
FF	0.05	0.12	yes
AR_LI	0.06	0.14	yes
Con_LI	(...)	0.06	(...)
Sol_LI	(...)	0.10	(...)
Circ_SC	(...)	0.12	(...)
Rec_SC	0.03	0.06	yes
FFa	0.05	0.12	yes
AR_F	0.07	0.16	yes
AR_SC	(...)	0.37	(...)
Reg	(...)	0.11	(...)

Extended Data Fig. 10 | Results of equivalence tests between sample IW and IU. Values represent the calculated minimum range *D*, under which the equivalence test would still be passed. If this value is equal or smaller than the threshold for curvi-planar ash grains (D_{max}, see also Extended Data Fig. 6), the compared data sets can be treated as significantly similar in the according shape parameter. Equivalence test results are only valid for data sets with homogeneous variances. If this precondition is not fulfilled, results were omitted, denoted by "(...)". In 12 of the tested 23 shape parameters, a significant similarity is verified via e-tests. In the other 11 shape parameters, no statement can be made.